

Highly-Efficient thin Film LiNbO₃ Surface Couplers Connected by Ridge-Waveguide Subwavelength Gratings

Sipan Yang

Shanghai Jiao Tong University <https://orcid.org/0000-0002-8833-4149>

Jinbin Xu

Shanghai Jiao Tong University

Yaqian Li

Shanghai Jiao Tong University

Liyang Wu

Shanghai Jiao Tong University

Xueling Quan

Shanghai Jiao Tong University

Liucheng Fu

Shanghai Jiao Tong University

Min Liu

Shanghai Jiao Tong University

Zhengjie Wang

Shanghai Jiao Tong University

Xiulan Cheng (✉ xlcheng@sjtu.edu.cn)

Shanghai Jiao Tong University <https://orcid.org/0000-0002-2552-464X>

Research Article

Keywords: film, lithium niobate, grating coupler, ridge waveguide, subwavelength grating

Posted Date: March 11th, 2021

DOI: <https://doi.org/10.21203/rs.3.rs-265413/v1>

License:   This work is licensed under a Creative Commons Attribution 4.0 International License.

[Read Full License](#)

Version of Record: A version of this preprint was published at Journal of Materials Science: Materials in Electronics on August 2nd, 2021. See the published version at <https://doi.org/10.1007/s10854-021->

06599-7.

Highly-efficient thin film LiNbO₃ surface couplers connected by ridge-waveguide subwavelength gratings

Sipan Yang^{1,2}, Jinbin Xu², Yaqian Li², Liying Wu², Xueling Quan², Liucheng Fu², Min Liu², Zhengjie Wang², Xiulan Cheng^{1,2,*}

¹ Department of Micro-nano Electronics, School of Electronic Information and Electrical Engineering, Shanghai Jiao Tong University, Shanghai 200240, China

² Center for Advanced Electronic Materials and Devices (AEMD), Shanghai Jiao Tong University, Shanghai 200240, P.R. China

Abstract: The ridge waveguide integrated grating couplers (GCs) in lithium niobate on insulator (LiNbO₃, LNOI) were designed, fabricated and characterized. Two ends of the gratings structures were connected through the middle photonic rib-waveguide of a sub-micrometric-diameter, which was nanostructured with the geometry of side-wall corrugated subwavelength gratings structure. A high coupling efficiency of -5.1 dB for the best thin film LiNbO₃ (TFLN) grating coupler was measured at the telecommunication wavelength of 1561 nm for quasi-transverse-electric (TE) polarized signals, with a broad 3-dB optical bandwidth of wider than 95 nm. All the devices structure patterns for the integrated LNOI GCs could be simultaneously defined by one step of electron-beam lithography, and then easily fabricated by the dry-etching processes. This compact component exhibited magnificent performance, and might show the potential functionalities for the TFLN-based integrated optical waveguide devices.

Key words: Thin film, lithium niobate, grating coupler, ridge waveguide, subwavelength grating

1. Introduction

Single crystal thin film lithium niobate (TF-LiNbO₃, TFLN) and LN-on-insulator (LNOI) wafer, have been emerging as an attractive platform for the applications of high-performance photonic integrated components (PICs), due to LN excellent properties of electro-optic, non-linear optics, high refractive index contrast between photonic waveguide core and its cladding, as well as the available wide optical transparency ranges from 0.4 to 5.2 μm [1-3]. Among all the light-coupling approaches, unlike to the edge couplers, surface grating couplers (GCs) were considered as the fundamental passive components, and have been widely explored for highly-efficient interfacing optical fiber to waveguide, especially for the increasing applications of optical waveguide devices and circuits [4-7]. For the existing researches

focused on the waveguide sub-wavelength structures such as the common structures of long-period diffraction gratings, Bragg gratings and short-period subwavelength gratings (SWG), the dispersion relation between frequency (f) and wavenumber (β) for respective gratings waveguide in the optical integrated devices had been investigated [8-10]. It was reported that waveguide SWG can be considered as a low-loss homogeneous medium when the effective wavelength is larger than the period of waveguide SWG [11]. SWG waveguide used as the Bragg gratings was simulated, in order to effectively suppress the side-lobes of transmission spectrum [12]. The short-period SWG nanostructured in the middle of SiO₂ microfiber was fabricated, and used to reduce the out-of-plane scattering and radiation losses [13]. The light propagation length was properly controlled in SWG waveguide structure to manipulate the light mode [14]. In addition, the SWG structures fabricated on LNOI had also been enormously investigated. For example, the tapered LNOI GCs connected via a few hundreds of micro-meters-length SWG waveguide was theoretically reported, and the integrated GCs with sidewall corrugated SWG geometry could be regarded as the band-rejection filter [15]. A non-linear LNOI optical element was fabricated by periodically altering the dimensions of short-period photonic-wire waveguide [16]. The long LNOI resonator structure integrated with both uniform and chirped SWG waveguide was fabricated to realize the nonlinear light-matter interaction in the fields of modulators [17].

However, the SWG structure embedded in the middle region of photonic-wire waveguide and used as a low-loss optical waveguide, has not been systematically investigated for the applications of light-coupling and propagation in LNOI, and the traditional TFLN GCs usually have a high insertion loss (IL). For instance, a minimum loss of -12 dB/coupler for transverse-electric (TE) polarization was measured at 1510 nm in the tapered GCs with silica cladding and bend bridged photonic-wire waveguide [18]. Multiple integrated GCs with different lengths of straight waveguide region were implemented, and exhibited a loss of around -9.95 dB/coupler at 1542 nm [19]. A coupling efficiency (CE) of around -7 dB/coupler was experimentally obtained at the wavelength of near 1550 nm for vertical coupling integrated GCs, and the hard-etching nature of z-cut TFLN device layer was fully etched in combination with the ultimate optimizations of geometrical structure and parameters [20]. Noticed that there ever reported a relatively low loss in LNOI GCs, but these improved GCs based on traditional structure were realized by conducting sufficient optimizations, including adding the oxide upper cladding or refractive index matching materials [18, 20], setting the highly-cost and complicated bottom reflector [21, 22], employing the curved focused chirped gratings with fully optimized geometrical parameters [23], requiring more complex structure design and fabrication processes [24], and simultaneously adopting multiple optimizations [25, 26]. Besides, the output performance of the existing integrated LNOI GCs were sensitive to the alignment-error and manufacturing process imperfections, as well as with a narrow 3-dB optical bandwidth (BW) [23, 24, 26]. Therefore, it is interesting to investigate the low-loss LNOI GCs with easy fabrication process for facilitating the large-scale production of PICs. In our work, the high-performance LNOI GCs integrated with waveguide SWG, have been designed and effectively fabricated. The proposed integrated GCs were of simple structure and ease of manufacturing. All the device structures monolithically defined in the chip can be patterned by one step electron-beam lithography (EBL), followed by dry-etching processes. The light coupling and transmission characteristics of LNOI GCs for TE mode have been systematically

investigated, and the performance in terms of device structural and optical properties for the fabricated GCs embedded with SWG have been characterized.

2. Simulations and experiments

The schematic top-view of the whole structure of rib-waveguide integrated LNOI GCs is shown in Fig. 1(a). Seen from Fig. 1(a), two ends of GCs were bridged by the middle structure of SWG waveguide, L_{gc} is the total length of a single end of straight ridge-waveguide gratings with a nominal width of w_{gc} . L_{taper} is the length of ridge-waveguide taper. Λ_{swg} is the periodicity of short-length SWG, w_{swg} is the width of a single SWG stripe, w_{swg}/Λ_{swg} is the filling factor of SWG (FF_{swg}). L_{swg} is the total length of SWG stripes, the bridging ridge-waveguide stripes structure is of periodic perturbation, Δw is the amplitude variation of SWG stripes. The enlarged cross-section of a part of ridge-waveguide GCs transmission model is shown in Fig. 1(b). Λ is the periodicity of diffraction grating stripes, w is the width of a single grating stripe, w/Λ is the filling factor of gratings (FF). The total thickness of TFLN device layer is $H=600$ nm, h is the etching depth of ridge waveguide. Seen from Fig. 1(b), it is clear to find that the injected light source was located on the top left and above the TFLN layer, the optical fiber core regraded as the sources and set to be tilted with an incident angle (θ_{inc}). M1 is the top power monitor used to record the original light diffracted downwards the GC, M2 is the power monitor used to record the light transmission through the left side, M3 is the power monitor used to record the light diffracted downwards the bottom substrate, and M4 is the power monitor used to record the light transmission through the right side.

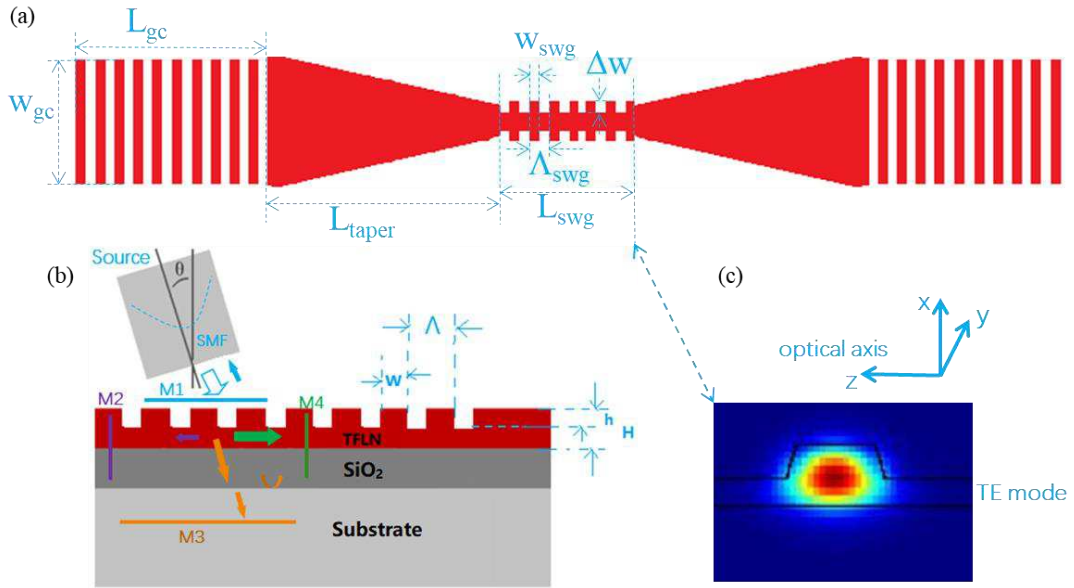


Fig. 1 Schematic of the proposed LNOI integrated GCs and the simulation details. **(a)** The top-view of ridge waveguide GCs integrated with SWG structure; **(b)** The simulated transmission spectra were recorded by the monitors as displayed with different color arrows, and the scanned transmissivity was plotted; **(c)** The simulated transverse-electric fields (E_z) distribution of light mode at 1550 nm in the middle photonic waveguide.

It was reported that the GCs performance experience a dependence on the devices design and parameters selections as well as actual fabrication [25, 27], to obtain a maximum CE product for the ridge-waveguide integrated LNOI GCs, the geometry and structure parameters of the proposed devices were fully considered such as the set of deeper etching depth of h for

a better light mode confinement, large diffraction grating period, and the corresponding duty cycle. As for the effective media theory and gratings diffraction conditions [28-31], the light-coupling processes for the whole GCs structure integrated with SWG was simulated (Lumerical, Ansys), and the geometrical parameters were fully optimized. To achieve single mode light propagation in photonic waveguide, the simulated transverse-electric fields (E_z) distribution operated at 1550 nm was obtained, as shown in Fig. 1(c). For the requirements of waveguide SWG structure, the relationship between Λ_{swg} and the light effective wavelength ($\lambda_{\text{eff}}=\lambda/n_{\text{eff}}$) was also studied, where n_{eff} is the effective index of waveguide SWG, λ is the propagation wavelength in vacuum. The resulting optimum parameters for the proposed integrated GCs were obtained and listed in Table 1. Λ_{swg} was optimized to be of 500 nm, L_{gc} was of 20.88- μm -long with 10.95- μm -width (w_{gc}), $\Delta w=0.2 \mu\text{m}$. L_{taper} was also fully optimized for effective mode adiabatic transition with a fixed lateral length of 200 μm . Besides, 500- μm -thick Si substrate was selected to support the bonded wafer, lower cladding of silicon dioxide was optionally selected to be of 4.7 μm by the simulations, and used as the bonding material in the LNOI wafer.

Table 1 Comparison of the simulated structure parameters and actual fabricated values for the ridge-waveguide LNOI GCs integrated with waveguide SWG.

Geometrical parameters	Λ	FF	Λ_{swg}	FF_{swg}	h
Simulated value	1160 nm	0.501	500 nm	0.511	503 nm
Fabricated value	1160 nm	0.510	506 nm	0.564	471 nm

In our experiments, all the ridge-waveguide optical components were simultaneously fabricated on the x-cut LNOI wafer (supplied by Nanolin). The LN crystallographic axes (x, y, z) is plotted with the solid blue arrows, and the optical axis is in z direction, due to the fact that the light propagates in +y direction for the purchased x-cut TFLN wafer, as inserted in Fig. 1(c). The customized LNOI wafer was firstly sliced into 1.0 \times 1.2 cm² segments, and the sample surface was fully cleaned by wet process. Then, the hard mask of amorphous silicon (α -Si) film with 800-nm-thick was deposited on the TFLN layer, followed by the positive electron-beam resist spin-coating with around 400-nm-thick. Afterwards, all the device structures patterns were monolithically defined by one step of electron-beam lithography (EBL) process (from Vistec EBPG 5200). Then, the standard etching process with SF₆ and C₄F₈ mixed gases by using inductively coupled plasma-reactive ion etching (ICP-RIE) tool was employed to etch the α -Si hard mask, and the residual resist was removed by wet etching with acetone solutions, and then the sample was treated with the oxygen plasma, followed by the improved schemes of multi-steps of Argon-ions etching process in ICP setups to transfer the patterns into the underlying LN film with an expected etching-depth. Accordingly, once the target LN ridge-waveguide structures was defined, and the residual α -Si hard mask was removed by the wet etching with diluted potassium hydroxide solutions, followed by the optimized surface cleaning process as developed in our group.

3. Measurements and discussions

The optical properties for the fiber-to-GC transmission was systematically investigated, and the product of E_z field distribution for TE polarized optical wave in the simulation region was analyzed, as presented in Fig. 2(a). Seen from Fig. 2(a), it is easy to find that there is a part of light diffracted downwards and further reflected upwards due to the SiO₂/Si interface, the small

input fiber angle of θ_{inc} was slant to reduce the backward reflection and realize the effective optical fiber-to-waveguide coupling [32, 33]. Noted that a part of light mode injected from optical fiber was effectively coupled into the GCs, further transmitted through the other end of ridge-waveguide. Meanwhile, there also existed the influence of partial light radiated downwards and further leaked into the bottom high-index Si substrate, owing to the fact that there is one of the mode loss sources in GCs [26]. According to the proposed model structure as shown in Fig. 1, the spectral response for the GCs operated in the telecom wavelength ranges was simulated. The spectra response was recorded by these four monitors, and the optical transmissivity were extracted, as plotted in Fig. 2(b), respectively. Seen from Fig. 2(b), it is clear to see that there is a peak value at 1550 nm for the M4 transmission curve, and it is corresponding to a minimum value for the M3 for our fully optimized GCs.

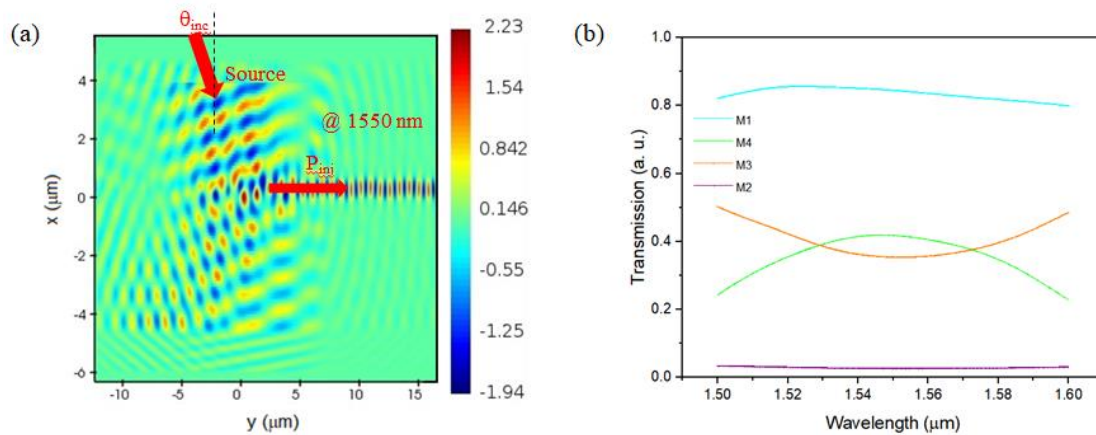


Fig. 2. Optical properties simulations for the proposed GCs. **(a)** The simulated light mode distributions of the x-cut LNOI integrated GCs operated at 1550 nm corresponding to a maximum CE. The origin of the coordinate axes was located at the leftmost end of the left taper in the model, and the input source of fiber core was launched at $x=+5.1 \mu\text{m}$ and $y=-7.8 \mu\text{m}$; **(b)** The simulated transmission spectra were recorded by the monitors as displayed in Fig. 1(b), and the scanned transmissivity was extracted and plotted with M1 (cyan curve), M2 (orange curve), M3 (purple curve) and M4 (green curve), respectively.

For the device structural characterizations of the fabricated integrated LNOI GCs, the measurements of optical microcopy, high resolution optical confocal laser scanning microcopy (LSM) were performed, and scanning electron microscope (SEM) characterizations were conducted at a proper voltage mode. The optical micrograph of partial GCs structure is presented in Fig. 3(a), and the enlarged LSM image of the gratings and taper structure is exhibited in Fig. 3(b). Seen from Fig. 3(b), we can find that the surface of the fabricated gratings structure is rough, which could be mainly attributed to the effects of etched LN re-deposition, the sputtered byproducts and particles, as well as the contaminations exist in the chamber during the fabrication processes, as referenced in literatures [27, 34]. It is clear to find that the sidewall of the etched ridge-waveguides and gratings structure is slant after fabrication, and the total size of deeply-etched ridge-waveguide gratings was measured to be of $11\text{-}\mu\text{m}$ -wide. The width of a single ridge-waveguide grating stripe was measured to be of about 595 nm, and the area of the measured GCs region was about $20.9 \times 11 \mu\text{m}^2$. The SEM image for the whole SWG structure is exhibited in Fig. 3(c), the measured width of a single ridge-waveguide SWG stripe was about 290 nm. All the measured results were basically in good agreement with the originally designed parameters, since the geometrical parameters

could be affected by the fabrication imperfections, especially for defining the fine grating and photonic-wire waveguide structures.

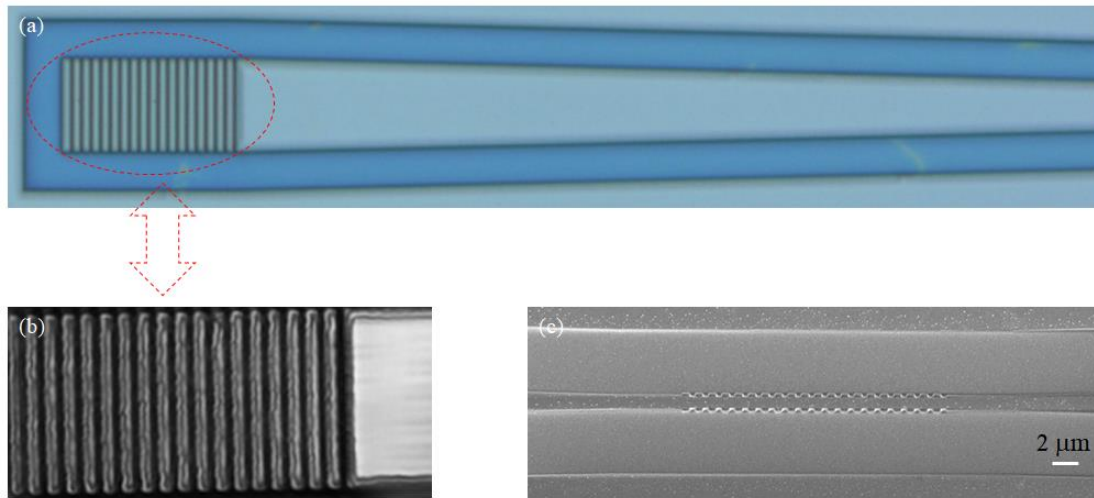


Fig. 3. The structure characterizations for the fabricated LNOI devices. **(a)** Optical image of the fabricated GCs and taper structure; **(b)** Enlarged LSM optical microscope graph of the uniform gratings layout; **(c)** SEM image of the partial device structure embedded with waveguide SWG.

For the measurements of optical transmissivity, the input signals originated from a tunable continuous-wave laser source (by Agilent TLS 81960A), and the optical power-meter (by Keysight 81636B) were employed to measure the transmission response for the fabricated integrated LNOI GCs. The schematic of the testing systems is plotted in Fig. 4. Seen from Fig. 4, we can find that the TE-polarized mode was emitted from the laser, the input laser power was fed into the devices by the optical fiber, and then the output transmission signals were collected by the optical spectrum analyzer for interfacing the standard single mode fiber (SMF) to GCs after multiple manual adjustments for reaching its maximum throughput. The concrete parameters in the measurement setups are presented as follows: the input laser power was set to be of 10 dBm, the operating wavelength was ranged from 1.504 μm to 1.621 μm, and the step size of sweeping wavelength was 2 pm. The mode of input light was adjusted by polarization controller. Considering that the optical fibers were fixed on the holder, and the position can be moved and precisely adjusted by the manipulator stage, but the relative incident angle (θ_{inc}) to the sample surface is fixed to be of 10° both in simulations and experiments, as for the case of actual availability in our measurement systems.

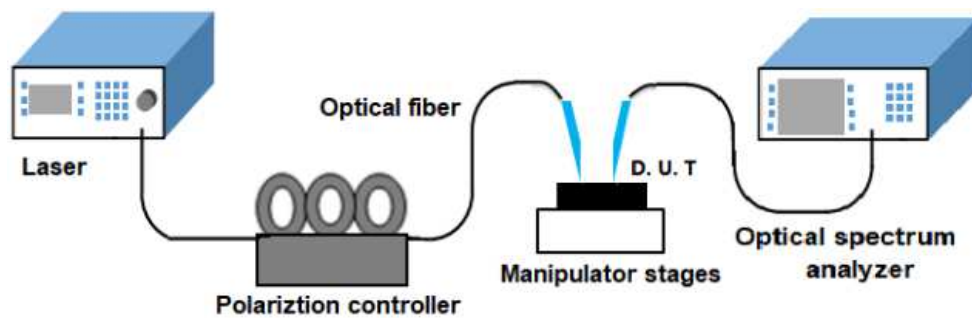


Fig. 4 Schematic of the optical testing systems employing several individual optical fibers. D. U. T: device under test.

The spectral response for the integrated GCs was measured, as shown in Fig. 5. Since multiple devices with the same structure and designed parameters were simultaneously

fabricated, and a series of devices measurement characterizations were conducted. The simulated transmissivity for the conventional GCs was plotted with the black line, and all the transmission curves were compared and analyzed. Seen from the transmission characteristics in Fig. 5, it is clear to find that a low loss of around -5.1 dB/coupler operated at 1561 nm was achieved in the best device, where the total losses include the coupling loss, the propagation loss, and any losses in the whole device. Noted that there was only a slight difference between these fabricated GCs, the average loss was calculated to be of -5.35 dB/coupler at a wavelength of 1550 nm, and the discrepancy might be due to the imperfect fabrication process. Meanwhile, the performances of all the fabricated devices designed with identical structure were stable, and the measured results revealed that the sample is homogenous. Since there was no set of cladding layer in our case, thus the efficiency can be further improved by depositing with proper upper cladding layer. It is obvious to find that the curve of CE slightly oscillates, which was attributed to the effect of the Fabry-Prot-like structure formed in GCs, as previously reported in literatures [12, 35]. The measurements experienced a large dependence on the pitches, and the peak wavelength was shifted a few nanometers for our fabricated GCs, which might be closely related to a lack of the best selection of θ_{inc} and due to the fabrication tolerance. In addition, the 3-dB optical bandwidth was also characterized with the dashed blue line, as shown in Fig. 5, and a broad 3-dB BW was extracted to be of more than 95 nm, which was limited by the intrinsic property in surface GCs structure and capabilities of our experimental setups.

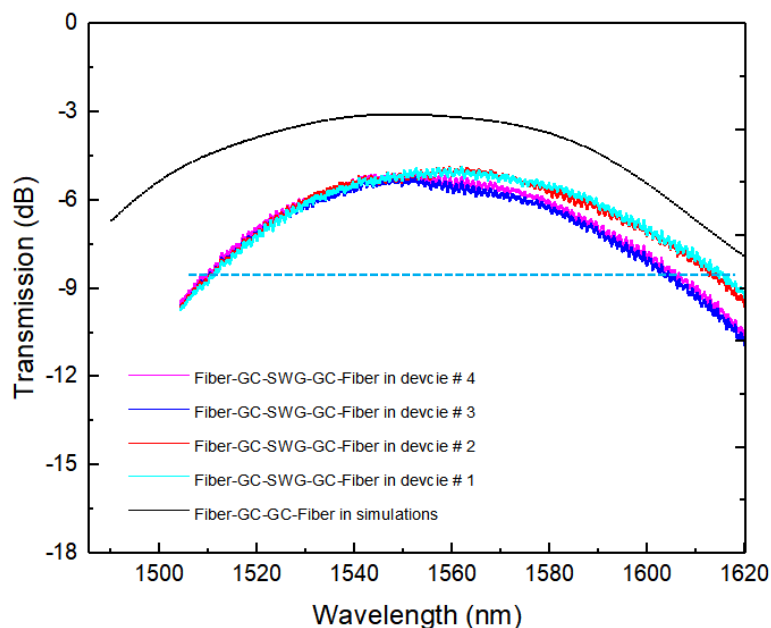


Fig. 5 The simulated (black line) and experimentally measured transmissivities of the ridge-waveguide GCs.

Compared with the existing researches of integrated LNOI GCs [20, 21, 26], our easily fabricated GCs integrated with waveguide SWG were highly-efficient, which could be mainly attributed to the contributions of self-designed LNOI-on-Si wafer, optimal geometrical parameters and improved manufacturing process. Since the preferable schemes of multi-steps etching within each single cycle was developed in our fabrication process, in combination with the improved cleaning process, due to the fact that experimental results highly depend on the fabrication tolerance and actual manufacturing processes, especially for the structure

parameters of h , and w . Besides, the obtained high performance GCs, which might be partly owing to the designed GCs with short-period SWG structure, thus the index of waveguide core could be effectively tuned, the out-plane scattering and radiate losses in LNOI ridge-waveguide were reduced, as revealed in the literatures [13, 28]. And it could not be denied that the scheme of GCs integrated with low-loss SWG waveguide is a good solution to obtain a high CE for effectively interfacing optical fiber and waveguide. In our following work, we will make great efforts to improve the output performance in a wide margin, and further optimize the GCs design and structure parameters with the full consideration of actual fabrication process, as well as properly solving the problems as mentioned above, then to yield the output performance close to the ideal model.

4. Conclusions

In conclusion, the ridge-waveguide LNOI integrated GCs with a high efficiency have been demonstrated. The fabricated integrated GCs were of simple structure, and embedded with the low-loss SWG waveguide in the middle region. The measured optical response for the best GC exhibited a low IL of -5.1 dB and a wide 3-dB bandwidth of around 95 nm. The fabrication process for our devices was easy to be completely patterned by one step of EBL, followed by dry-etching with complementary metal oxide semiconductor (CMOS) compatible processes. The results may greatly boost the large scale production of surface coupling for photonic waveguide devices.

Declaration of Competing Interest

There is no competing interest to declare.

Acknowledgements

This work was supported by the fund of Shanghai Committee of Science and Technology (No. 18DZ2295400), and the authors would like to acknowledge SJTU-AEMD for support.

References

1. G. Poberaj, H. Hu, W. Sohler, P. Gunter, Lithium niobate on insulator (LNOI) for micro-photonic devices. *Laser Photon. Rev.* **6**, 488-503 (2012).
2. R. S. Weis, T. K. Gaylord, Lithium niobate: summary of physical properties and crystal structure. *Appl. Phys. A* **37**, 191-203 (1985).
3. P. Rabiei, J. Ma, S. Khan, J. Chiles, S. Fathpour, Heterogeneous lithium niobate photonics on silicon substrates. *Opt. Express* **21**, 25573-25581 (2013).
4. H. Subbaraman, X. Xu, A. Hosseini, X. Zhang, Y. Zhang, D. Kwong, R. T. Chen, Recent advances in silicon-based passive and active optical interconnects. *Opt. Express* **23**, 2487-2510 (2015).
5. M. He, M. Xu, Y. Ren, J. Jian, Z. Ruan, Y. Xu, S. Gao, S. Sun, X. Wen, L. Zhou, L. Liu, C. Guo, H. Chen, S. Yu, L. Liu, X. Cai, High-performance hybrid silicon and lithium niobate Mach-Zehnder modulators for 100 Gbit s⁻¹ and beyond. *Nat. Photon.* **13**, 359-364 (2019).

6. M. Xu, M. He, H. Zhang, J. Jian, Y. Pan, X. Liu, L. Chen, X. Meng, H. Chen, Z. Li, X. Xiao, S. Yu, S. Yu, X. Cai, High-performance coherent optical modulators based on thin-film lithium niobate platform. *Nat. Commun.* **11**, 3911 (2020).
7. W. Xiong, G. Wang, J. Li, C. Zhao, W. Wang, H. H. Radamson, SiN-based platform toward monolithic integration in photonics and electronics. *J. Mater. Sci.: Mater. Electron.* **32**, 1-18 (2021).
8. R. Halir, P. J. Bock, P. Cheben, A. Ortega-Moñux, C. Alonso-Ramos, J. H. Schmid, J. Lapointe, D. X. Xu, J. G. Wangüemert-Pérez, Í. Molina-Fernández, S. Janz, Waveguide sub-wavelength structures: a review of principles and applications. *Laser Photon. Rev.* **9**, 25-49 (2014).
9. U. Moura, Y. Bustamante, G. Farias, B. Snyder, A. Miller, J. V. Campenhout, P. Absil, Design and optimization of subwavelength silicon photonics edge coupler for cleaved fibers SWG. 2018 SBFoton International Optics and Photonics Conference (SBFoton IOPC), (2018).
10. L. Chrostowski, H. Shoman, M. Hammood, H. Yun, J. Jhoja, E. Luan, S. Lin, A. Mistry, D. Witt, N. A. E. Jaeger, S. Shekhar, H. Jayatileka, P. Jean, S. B-de Villers, J. Cauchon, W. Shi, C. Horvath, J. N. Westwood-Bachman, K. Setzer, M. Aktary, N. S. Patrick, R. J. Bojko, A. Khavasi, X. Wang, T. F. de Lima, A. N. Tait, P. R. Prucnal, D. E. Hagan, D. Stevanovic, A. P. Knights, Silicon photonic circuit design using rapid prototyping foundry process design kits. *IEEE J. Sel. Top. Quantum Electron.* **25**, 8201326 (2019).
11. M. Zhang, C. Wang, R. Cheng, A. Shams-Ansari, M. Loncar, Monolithic ultra-high-Q lithium niobate microring resonator. *Optica* **4**, 1536-1537 (2017).
12. E. F. Zhanghua Han, Sailing He, Surface plasmon Bragg gratings formed in metal-insulator-metal waveguide. *IEEE Photon. Technol. Lett.* **19**, 91-93 (2007).
13. M. Ding, M. N. Zervas, G. Brambilla, A compact broadband microfiber Bragg grating. *Opt. Express* **19**, 15621-15626 (2011).
14. R. Zia, M. D. Selker, P. B. Catrysse, M. L. Brongersma, Geometries and materials for subwavelength surface plasmon modes. *J. Opt. Soc. Am. A* **21**, 2442-2446 (2004).
15. M. A. Baghban, J. Schollhammer, C. Errando-Herranz, K. B. Gylfason, K. Gallo, Bragg gratings in thin-film LiNbO₃ waveguides. *Opt. Express* **25**, 32323-32332 (2017).
16. C. Wang, X. Xiong, N. Andrade, V. Venkataraman, X. F. Ren, G. C. Guo, M. Loncar, Second harmonic generation in nano-structured thin-film lithium niobate waveguides. *Opt. Express* **25**, 6963-6973 (2017).
17. M. H. Mengyue Xu, Siyuan Yu, Xinlun Cai, Thin-film lithium niobate modulator based on distributed Bragg grating resonators. Asia Communications and Photonics Conference (ACP), (2019).
18. S. G. Mohamed Mahmoud, Gianluca Piazza, Lithium niobate on insulator (LNOI) grating couplers. CLEO: Science and Innovations 2015, (2015).
19. J. S. Mohammad Amin Baghban, Carlos Errando-Herranz, Kristinn B. Gylfason, Katia Gallo, Waveguide gratings in thin-film lithium niobate on insulator. The European Conference on Lasers and Electro-Optics 2017, (2017).
20. A. Kar, M. Bahadori, S. Gong, L. L. Goddard, Realization of alignment-tolerant grating couplers for z-cut thin-film lithium niobate. *Opt. Express* **27**, 15856-15867 (2019).

21. Z. H. Chen, R. H. Peng, Y. W. Wang, H. B. Zhu, H. Hu, Grating coupler on lithium niobate thin film waveguide with a metal bottom reflector. *Opt. Mater. Express* **7**, 4010-4017 (2017).
22. Z. H. Chen, Y. W. Wang, Y. P. Jiang, R. R. Kong, H. Hu, Grating coupler on single-crystal lithium niobate thin film. *Opt. Mater.* **72**, 136-139 (2017).
23. Z. Chen, Y. Ning, Y. Xun, Chirped and apodized grating couplers on lithium niobate thin film. *Opt. Mater. Express* **10**, 2513-2521 (2020).
24. M. S. Nisar, X. Zhao, A. Pan, S. Yuan, J. Xia, Grating coupler for an on-chip lithium niobate ridge waveguide. *IEEE Photon. J.* **9**, 6600208 (2017).
25. I. Krasnokutska, R. J. Chapman, J. J. Tambasco, A. Peruzzo, High coupling efficiency grating couplers on lithium niobate on insulator. *Opt. Express* **27**, 17681-17685 (2019).
26. L. T. Cai, and G. Piazza, Low-loss chirped grating for vertical light coupling in lithium niobate on insulator. *J. Opt.* **21**, 065801 (2019).
27. C. Wang, M. Zhang, X. Chen, M. Bertrand, A. Shams-Ansari, S. Chandrasekhar, P. Winzer, M. Loncar, Integrated lithium niobate electro-optic modulators operating at CMOS-compatible voltages. *Nature* **562**, 101-104 (2018).
28. J. A. Kubby, J. H. Schmid, G. T. Reed, P. J. Bock, P. Cheben, W. Sinclair, J. García, S. Janz, J. Lapointe, G. C. Aers, D. Poitras, Y. Li, G. Lopinski, A. Delâge, A. Densmore, B. Lamontagne, R. Ma, D. X. Xu, Applications of subwavelength grating structures in silicon-on-insulator waveguides. *Proc. SPIE* 7606, 76060F(2010).
29. Q. Xu, Y. X. Shao, R. Q. Piao, F. Chen, X. Wang, X. F. Yang, W. H. Wong, E. Y. B. Pun, D. L. Zhang, A theoretical study on rib-type photonic wires based on LiNbO_3 thin film on insulator. *Adv. Theor. Simul.* **2**, 1900115 (2019).
30. A. Hocini, T. Boumaza, M. Bouchemat, F. Royer, and J. J. Rousseau, Phase matched magneto optical single mode rib waveguides based on geometrical adjustments. *AEU-Int. J. Electron. Commun.* **64**, 1042-1045 (2010).
31. A. Kaushalram, S. A. Samad, G. Hegde, S. Talabattula, Tunable large dispersion in hybrid modes of lithium niobate-on-insulator multimode waveguides. *IEEE Photon. J.* **11**, 1-8 (2019).
32. C. Zhang, J. H. Sun, X. Xiao, W. M. Sun, X. J. Zhang, T. Chu, J. Z. Yu, Y. D. Yu, High Efficiency grating coupler for coupling between single-mode fiber and SOI waveguides. *Chin. Phys. Lett.* **30**, 014207 (2013).
33. L. Yu, L. Liu, Z. Zhou, X. Wang, High efficiency binary blazed grating coupler for perfectly-vertical and near-vertical coupling in chip level optical interconnections. *Opt. Commun.* **355**, 161-166 (2015).
34. L. He, M. Zhang, A. Shams-Ansari, R. Zhu, C. Wang, L. Marko, Low-loss fiber-to-chip interface for lithium niobate photonic integrated circuits. *Opt. Lett.* **44**, 2314-2317 (2019).
35. X. Chen, C. Li, C. K. Y. Fung, S. M. G. Lo, H. K. Tsang, Apodized waveguide grating couplers for efficient coupling to optical fibers. *IEEE Photon. Technol. Lett.* **22**, 1156-1158 (2010).

Figures

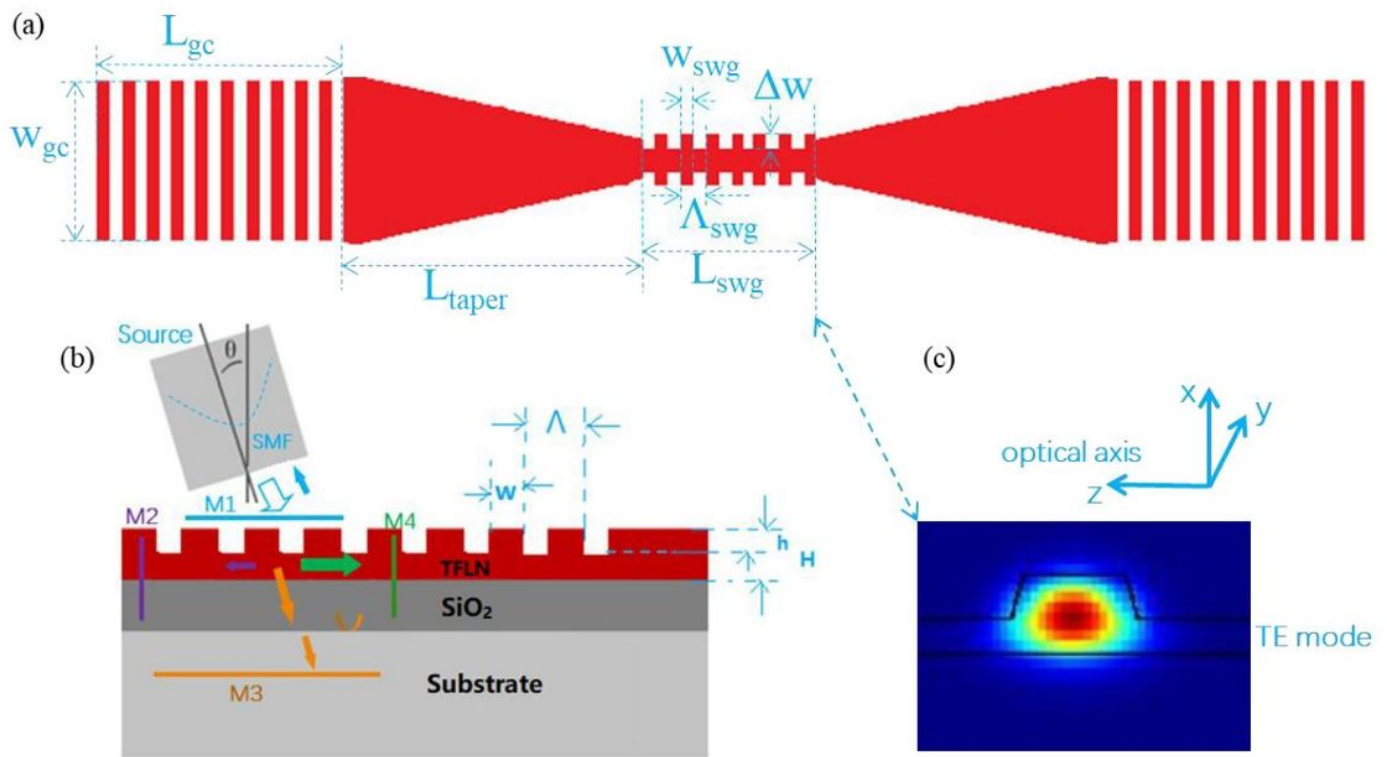


Figure 1

Schematic of the proposed LNOI integrated GCs and the simulation details. (a) The top-view of ridge waveguide GCs integrated with SWG structure; (b) The simulated transmission spectra were recorded by the monitors as displayed with different color arrows, and the scanned transmissivity was plotted; (c) The simulated transverse-electric fields (E_z) distribution of light mode at 1550 nm in the middle photonic waveguide.

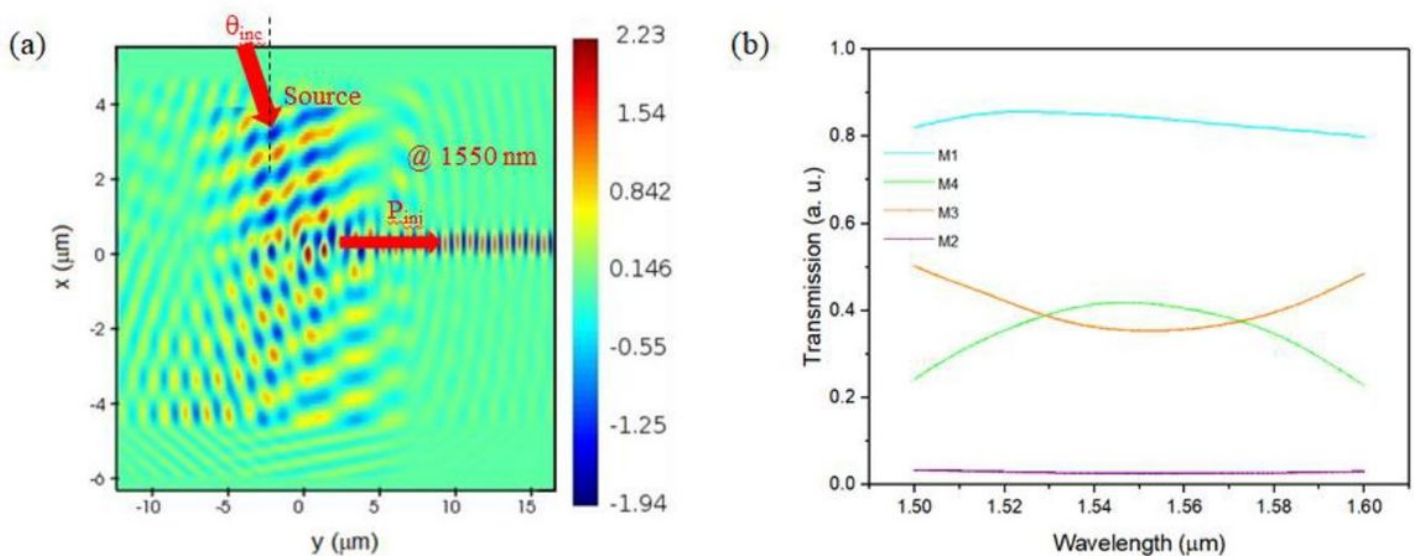


Figure 2

Optical properties simulations for the proposed GCs. (a) The simulated light mode distributions of the x-cut LNOI integrated GCs operated at 1550 nm corresponding to a maximum CE. The origin of the coordinate axes was located at the leftmost end of the left taper in the model, and the input source of fiber core was launched at $x=+5.1 \mu\text{m}$ and $y=-7.8 \mu\text{m}$; (b) The simulated transmission spectra were recorded by the monitors as displayed in Fig. 1(b), and the scanned transmissivity was extracted and plotted with M1 (cyan curve), M2 (orange curve), M3 (purple curve) and M4 (green curve), respectively.

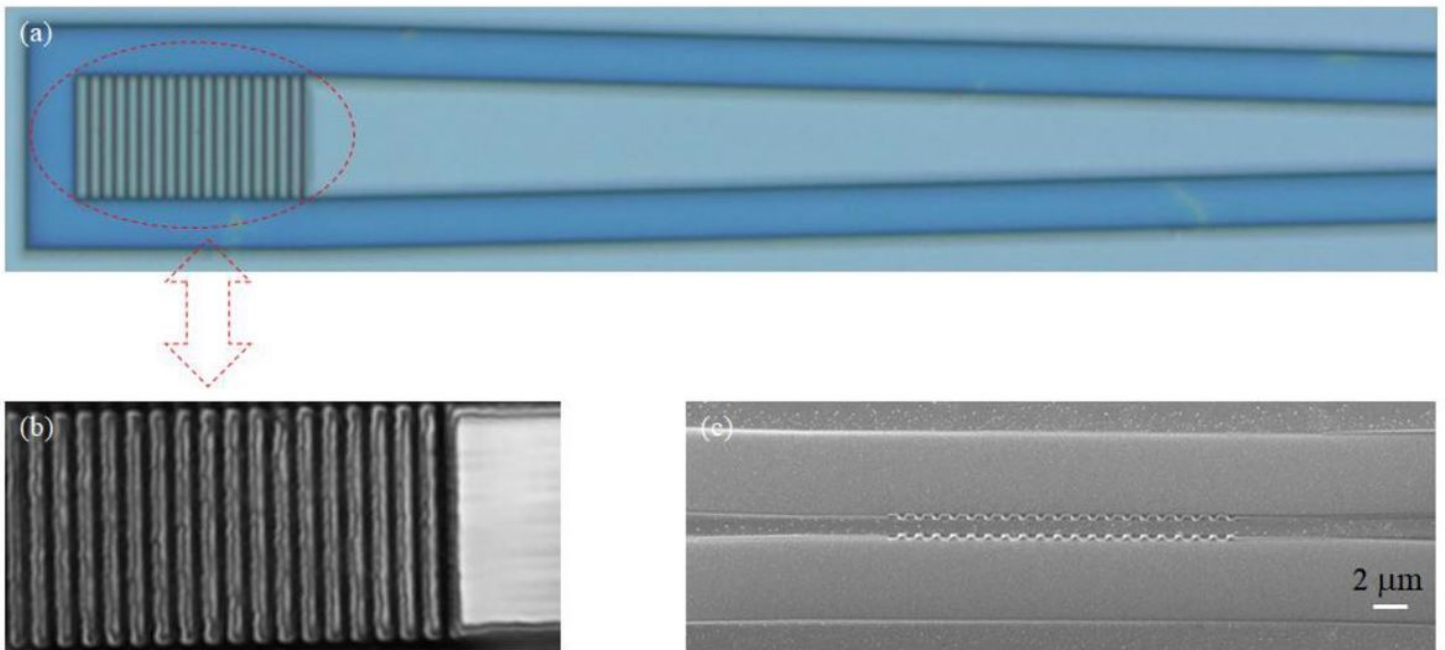


Figure 3

The structure characterizations for the fabricated LNOI devices. (a) Optical image of the fabricated GCs and taper structure; (b) Enlarged LSM optical microscope graph of the uniform gratings layout; (c) SEM image of the partial device structure embedded with waveguide SWG.

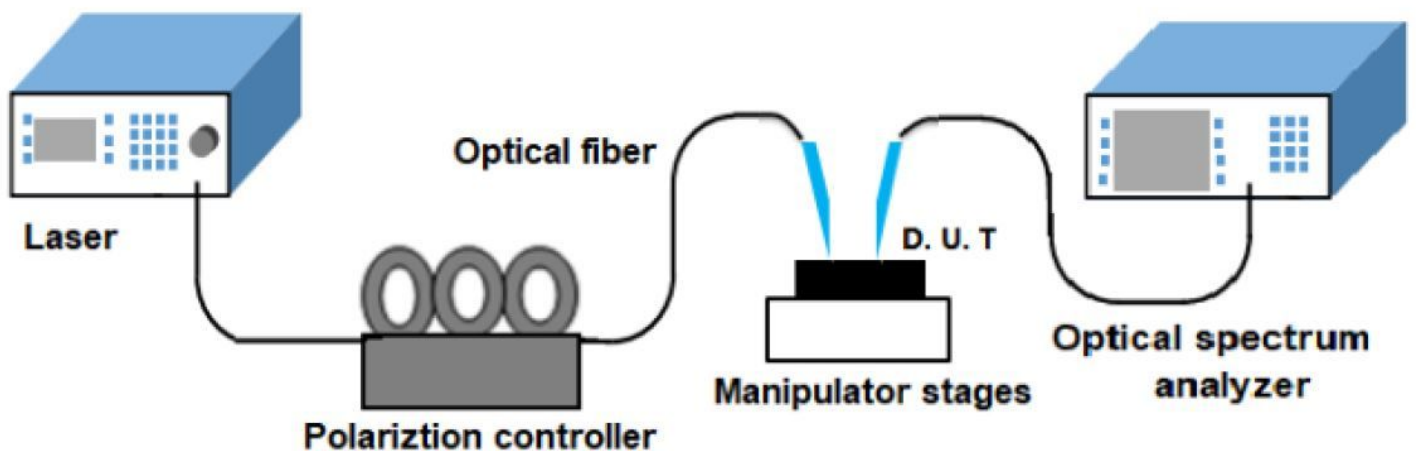


Figure 4

Schematic of the optical testing systems employing several individual optical fibers. D. U. T: device under test.

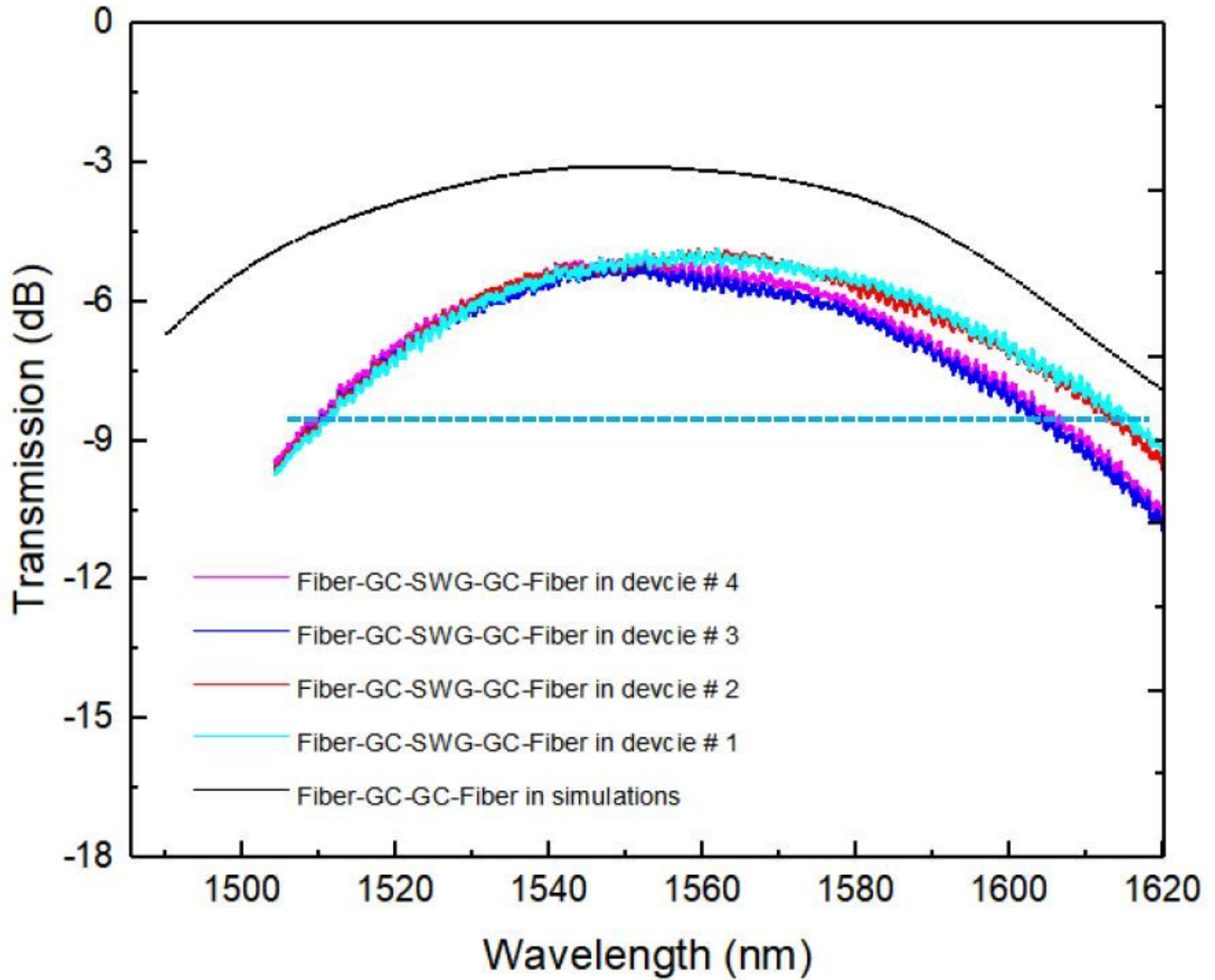


Figure 5

The simulated (black line) and experimentally measured transmissivities of the ridge-waveguide GCs.